Comparison of SLM cpTi sheet-TPMS and trabecular-like strut-based scaffolds for tissue engineering

Carmen Torres-Sanchez, James M. Borgman, Ben Sargeant, Hugo Bell, Enrique Alabort, Craig Lindsay, Paul P. Conway*

Dr. Carmen Torres-Sanchez, James M. Borgman, Ben Sargeant, Hugo Bell, Prof. Paul P. Conway
Multifunctional Materials Lab, Wolfson School, Loughborough University, Leics, UK
Email: c.torres@lboro.ac.uk

Dr. Enrique Alabort
Alloyed Ltd, Unit 15, Oxford Industrial Park, Yarnton, OX5 1QU, UK

Craig Lindsay
Core Specialist Services Ltd, Unit 4, Grandholm Crescent, Aberdeen, AB22 8AA

Keywords: cpTi, SLM, gyroids, IWP, Voronoi-tessellations, trabecular, osteoblasts

Abstract

This systematic comparison between sheet-based-TPMS and strut-based ordered and disordered Lattice topologies offers insights into parametric designs for tissue engineering scaffolds intended as implants in regenerative medicine. The study explores the effect of topology on compressive properties and in vitro osteoblastogenesis. TPMS-sheet Gyroid and IWP, Voronoi-tessellation with varying levels of sharpness and BCC-orthogonal Lattices were studied. Disparities between the design intent and the as-manufactured scaffolds that are intrinsic to the SLM manufacturing process are considered to ensure actual porosity and surface-area-per-unit-volume, two important factors in tissue engineering, are consistent across the set. Surface analysis reports the presence of a micro-porosity created by partly-sintered cpTi particles. The TPMS topologies display a stretching-dominated deformation and the strut-based disordered ones a bending-dominated double-shear failure. Although the trabecular-like structures exhibit an enhanced compressive behaviour when the designed

topology was smoothed, they are more prone to printing imperfections with the sharper finishes. The in vitro studies reveal that the trabecular-sharp topology displays a faster proliferation rate, explained by concavity-driven cellular growth, but its smooth counterpart promotes a larger differentiation extent, outperforming TPMS, as it is aided by larger pore throats lined with a micro-porosity at the scale of osteoblastic geometric features.

1. Introduction

An opportunity is offered by porous structures as implants in medical applications and arthroplasties because their mechanical and physical properties can be tuned to match patient-specific needs. For ex-vivo research, there is merit in using 3D models instead of 2D layers in tissue engineering to recapitulate cell growth in microenvironments that are similar to native tissue, because this narrows the gulf between in vitro tests and clinical translation [1]. Titanium and its alloys have been researched extensively because of their biocompatibility, high strength, low wear, corrosion resistance (due to the passivating oxide layer spontaneously formed on the surface[2]). When embodied as porous structures, they offer mechanical properties that can match those of cortical and trabecular bone[3], avoiding stress-shielding and biomechanical failure. Porous scaffolds must be conducive to osseointegration by means of providing channels and interconnected pores for nutrient distribution[4], networks for cellular proliferation, differentiation and maturation, and ultimately for bone healing[5].

Much work has explored different pore architectures and sizes, and routes by which they can be physically realised. Advances in CAD, multiphysics modelling[6] and additive manufacturing (AM) technology have allowed the definition of a design space to digitally test manufacturability boundaries for porous structures with the desired physical, mechanical and permeability properties that could enhance biological behaviour[7]. Techniques such as

Selective Laser Melting (SLM) or Electron Beam Melting (EBM) have been demonstrated as practical processing routes to achieve both parametric and non-parametric designs, ordered or random, using metals. With regards to parametric designs, Triply Periodic Minimal Surface (TPMS) structures[8] have received attention in recent years since AM managed to realise the manufacture of these topologies that offer mechanical superiority due to a uniformly distributed load transfer, free of discontinuities and self-intersecting elements, and therefore less prone to printing imperfections. Research to date has explored TPMS as a promising topology to emulate bone function. Parametric designs can also generate (pseudo-)random structures, e.g., trabecular-like. These structures remain attractive designs because they are based on the design principle that function follows form. It is accepted that there is a lack of systematic comparisons that comprehensively include the design of the porous structures and both their mechanical and biological performance, derived from that topology design [9].

The ultimate design intent for a structure to be successful in tissue engineering applications needs to accommodate a set of 'hygiene factors' that include a non-cytotoxic material; a pore size larger than 300 μm[4], more typically larger than 600 μm for in vivo applications[10], to promote osteoconduction; porosity larger than 50%[4], typically larger than 60% in commercial trabecular metal products [7a] to promote permeability as well as maintaining mechanical integrity to sustain physiological loads, esp. for load-bearing applications. Another important property of the tissue engineering embodiment is a high surface-to-volume ratio available for scaffold-cell interaction and implant-bone fixation[5]. Little attention has been given to the effect of pore morphology independent from surface area. Many studies have dealt with changes in pore size and/or porosity while keeping one of them constant, however surface area would vary as a consequence[10-11]. A systematic study where surface area is kept constant and pore morphology varied would help elucidate the true effect of pore size and porosity on cellular behaviour. Therefore, the coupled consideration of macro-

porosity (defined by the pore geometry and topology) and micro-porosity (by the small pores and wall roughness) [1a, 5] is relevant and important.

This present study provides a systematic comparison between parametric designs (two sheet-based TPMS topologies Gyroid and IWP, selected for their high permeability [12]) and a Voronoi-tesselation with two degrees of smoothening, chosen for biomimicry[13]) as well as a non-parametric orthogonal BCC Cubic-Lattice to establish the true contribution of pore topology to mechanical and in vitro performance. Unlike other studies, the design intent focused on porosity and surface area, rather than on pore size. The scaffolds were manufactured by SLM using cpTi and their physical, geometrical, compressive and osteoconductive properties were evaluated. Deviations between the design intent and the as-manufactured scaffolds, arising from the printing technique, created a micro-porosity and disparities in physical and geometrical features. Topology and micro-porosity were both considered to elucidate their effect on both mechanical performance and osteoblastogenesis over a long-term study of 28 days.

2. Methods and Materials

2.1. Design of the scaffold structure and measurements

The selected structures were two sheet-based TPMS (Gyroid and IWP) and two strut-based Trabecular (Sharp and Smooth) types. Preliminary studies considered other designs (e.g., Primitive and Diamond) but it was not technically possible to warrant the desired levels of open porosity and percolation due to pore occlusion in those designs. For comparative purposes, particularly in relation to mechanical and biological performance, a strut-based cubic lattice was also designed. The intended porosity was 75% with an intended surface area per unit volume in the range 30-40 cm^{-1}. Since porosity and surface area were the two

parameters intended to be consistent, the pore and strut sizes were varied depending on the unit cell design. The TPMS structures were generated in Grasshopper (Rhino 6.0., USA) using **Equations 1 and 2** without further topology optimisation:

Gyroid:

$$\cos(x)\sin(y) + \cos(y)\sin(z) + \cos(z)\sin(x) = 0 \quad (1)$$

IWP:

$$2[\cos(x)\cos(y)+\cos(y)\cos(z) + \cos(z)\cos(x)] - [\cos(2x) + \cos(2z) + \cos(2y)]=0 \quad (2)$$

These structures were generated from designated unit-cells. The surfaces were thickened in Magics v.22.03 (Materialise, Belgium) to achieve the intended porosity and surface area. The cubic lattice was generated by repeating a 1.4 mm 'cross' with a 0.81 mm overlap, that created the unit cell.

The trabecular structures used the Voronoi-Tessellation method of the Rhino software package **(Figure 1)**. First, a cube region, whose outer surfaces defined the overall volume of the porous scaffold, was generated. A random cloud of points was distributed within that volume. These points acted as seeds to create a 3D Voronoi tessellation within that volume. The edges of the Voronoi structure were then used to define a series of surfaces that formed the porous structure. To generate polyhedron cells, separated from each other at a distance proportional to the Voronoi cell structure, the 3D Voronoi structure was broken into points, edges and faces to allow an equidistant copy of these at an offset, which controlled the strut thickness and thus the relative density of the lattice structure. Finally, the Volume within the surfaces was 'filled' to create the solid trabecular structure, which generated the strut-based Trabecular 'Sharp' (T-Sharp) porous structure. An additional step was employed to generate the Trabecular 'Smooth' (T-Smooth) structure using the Catmull-Clark algorithm subdivision

smoothing step built into Rhino's 'Weaverbird'. The number of the nucleating points (or seeds) was controlled such that the lattice surface area to volume ratio could be modified for a constant porosity. No topology optimisation was performed.

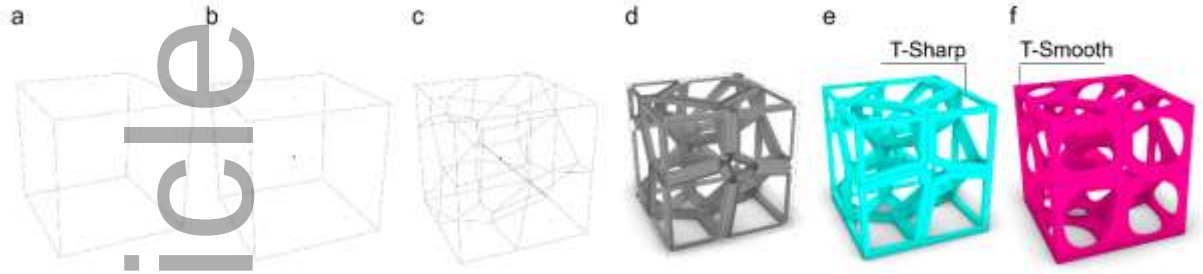

Figure 1. Design of the strut-based Trabecular model: a) bounding volume; b) random point generation (n=10 in this example); c) Voronoi tessellation; d) surface generation; e) volume generation to produce a 'Sharp' design; f) Catmull-Clark smoothening to generate a 'Smooth' design

2.2. Manufacture of the scaffolds

The scaffolds were prepared using commercially pure Titanium (cpTi) grade 1 powder in a SLM additive manufacturing process. The spherical gas-atomised powder (AP&C, GE Additive, Canada) displayed a distribution in the range 45 to 15 μm of D10 (19 μm), D50 (34 μm), D90 (47 μm), as per testing method ASTM B822-17; a chemical composition: (wt. %) C (0.01), O (0.10), N (0.01), H (0.002), Fe (0.03) Other (<0.2), as per ASTM E1941-10, E1409-13, E1447-09, E2371-13, and of density 2.63 g/cm^3, as per ASTM B212-17.

The SLM process was conducted in a TruPrint 1000 LMF (Trumpf, Germany) equipped with a 200 W Nd:YAG solid-state laser of 55 μm spot size under argon atmosphere (<100 ppm oxygen content). The preliminary study that established the printing parameters can be found in Supporting Information. The laser scanning parameters used were laser beam power of 140 W at a speed of 1,414 mm/s, a hatch distance of 0.11 mm and a layer thickness of 0.03 mm to

achieve volumetric energy density of 30 J/mm^3. A zig-zag scanning strategy with 90° rotation between layers, with a border offset of 0.05 mm was utilised. There were three sets of printed scaffolds on Titanium build-plates to suit the subsequent measurements and characterisation methods: set 1, used for mechanical testing and μCT reconstruction, cubes of side 10 mm, including a subset with 2-mm top/bottom solid layers, as per BS ISO 13314; set 2, used for wall roughness measurements via mercury injections, cylinders of 10 mm diameter and 10 mm height; set 3, for biological studies, short cubes of 10 x 10 mm base and 2 mm height. The scaffolds were excised (IsoMet High Speed Saw, Buehler, Germany) and ground (AutoMet 250, Buehler, Germany) using SiC paper 180 and 240 grit for 10-15 s to achieve parallel planes. The scaffolds were then ultrasonically cleaned in a sequential routine of soapy water (2 h), acetone (1.5 h) and 2-isopropanol (1.5 h) (Alfa Aesar, UK) to remove impurities and loose particles.

2.3. Measurements of models, physical characterisation and volumetric measurements

Volume (V_L), surface area, pore size, wall thickness or strut size of the CAD models were measured using Blender v2.92. The porosity in the as-designed models was calculated as the ratio V_L/V, where V_L is the volume of the porous scaffold, and V is total volume. The total porosity of the as-manufactured scaffolds was measured using (1-*D*), *D* being the density calculated as the ratio mass divided by volume, i.e., 'dry porosity'. The open porosity was measured using the Archimedes's method with acetone, a low surface tension liquid, as the immersion medium. Cubes (10x10x10 mm) were scanned in a μCT system (XT H 160 Xi-Tek, Nikon Metrology, UK) with 8.64 μm resolution at 100 kV and 90 μA. The acquisition was obtained by angular rotation of 0.12° and without beam hardening. 3015 two-dimensional images were collected for each specimen and the volumetric reconstruction was achieved in VG Studio Max 3.1 (Volume Graphics GmbH, Germany). The volumes were exported,

segmented and reconstructed in Fiji [14] to generate a STL file. The image stack was binarized, thresholded and resampled at factor 4. These parameters were optimised for consistency amongst the sets and to ensure features of wall roughness were not lost from the original μCT scan resolution. The pore size and wall thickness or strut size were measured in Fiji using the 2D stacks. The volumetric representations were used for surface area and contour size (i.e., mesh size) measurements in Blender (Blender v2.92). Gaussian local curvature on both the models and reconstructed volumes was measured in MatLab (R2019a, Mathworks, UK) analysing with '*pathcurvature*' function.

Observation of scaffold cross-sections was done by electron microscopy (FESEM JSM 7800F, JEOL, Japan) at an accelerating voltage of 5 kV. To assess the micro-porosity on the walls of the manufactured scaffolds, mercury injection was performed using an Autopore-IV 9500 porosimeter (Micromeritics Instrument Corp, USA) to determine pore throat size distribution and generate specific cumulative pore area as a function of pore throat size to give an indication of total available surface area to the pre-osteoblasts. Mercury was injected into the sample at incremental pressure steps from 1.5 to 500 psia using air then hydraulic oil as the displacing medium until equilibrium (i.e., the rate of intrusion drops below 0.001 μL/g-s), which was equivalent to 1 μm pore throat size when all injection ceased.

2.4. Mechanical Characterisation

Quasi-static compression testing was performed as per BS ISO 13314 standard using a UTM (Instron 3369, UK) with a 50 kN (Instron 2530-445, UK) load cell. A constant strain rate of $0.1\%.s^{-1}$ was applied, and the displacement of the top platen was measured with an LVDT (Instron 2601-062, UK) to reduce compliance errors. Samples were loaded in monotonic compression and increasing strain tests were carried out for validation. Recordings of the

compression were captured in 1080P HD using a Nikon D850 camera and DIC measurements were performed using an open source 2D digital image correlation for MatLAB (Ncorr v1.2). Strain was calculated as the LVDT displacement divided by the original specimen's height. Stiffness was calculated from the linear slope displayed in the elastic region of the stress-strain curves. Compression strength was calculated using the 0.2%-strain-offset method.

2.5. Biological Performance

The scaffolds were sterilized twice in an autoclave at 121 °C for 1 h followed by thorough rinsing with deionised sterile water. The scaffolds were pre-conditioned by soaking in culture media overnight. MC3T3-E1 murine pre-osteoblasts were cultured in standard flasks (ThermoFisher, UK) with essential α-MEM cell media (Gibco, UK), supplemented with 10% FBS (Gibco, UK), 1% L-Glutamine (Gibco, UK) and 1% Penicillin-Streptomycin (Gibco, UK). Pre-osteoblasts were incubated at 5% CO_2 and 37 °C (Thermo Scientific Heracell™ 150, UK), and used at passage 15. After reaching 70-80% confluence, pre-osteoblasts were detached using trypsin-EDTA (0.25% w/v trypsin/0.2% EDTA, Gibco) and the cellular solution was centrifuged (150 x g, 5 min). After preliminary studies to optimise 3D seeding efficiency (Supporting information), 1.8 x 10^5 pre-osteoblasts were seeded onto the pre-conditioned scaffolds in low adhesion 24-multiwell plates (Corning Costar®, UK). The media was topped up to 1mL. Cellular culture medium was replaced every 2 days for the duration of the experiment.

Cellular attachment and proliferation were monitored using a viability reagent (PrestoBlue™, Invitrogen, ThermoFisher Scientific, UK) over a 13-day period. This assay utilises a blue, non-fluorescent, cell-permeable, non-toxic and resazurin-based compound, that upon entering live cells is reduced to resorufin, a red compound that is highly fluorescent. Due to its light

sensitivity and to prevent over exposure of cells to PrestoBlue reagent, two plates were used in parallel, to maximise the number of consecutive timepoints and ensure robustness in the results. Cellular attachment was quantified as per the pre-osteoblasts attached to the scaffolds in the first 24 h of culture. The remaining 12 days in the period were used to determine the metabolic activity and determine the phenotypical switch point from proliferation to differentiation of this cell line within these scaffolds. As per the manufacturer's protocol, 500 μL of PrestoBlue™ media was added to each sample and left to incubate in a humidified environment for 90 min in the absence of light. 150 μL of media was then transferred to a black, clear-bottom 96-well plate (Corning, UK) for fluorescence analysis, using a spectrophotometer (Fluostar® Omega, UK) (Ex:560/Em:590). A cell standard line was used to transform fluorescence values into cell numbers. Cellular observation was done at 24 h from seeding and by fixation of the pre-osteoblasts (1 h immersion in 4% Paraformaldehyde (Sigma-Aldrich, UK)). These were then stained by immersion in a 1:1000 Phalloidin (Invitrogen, ThermoFisher, UK)-PBS (Gibco, UK) solution for 1 h followed by immersion in a 1:2500 DAPI (4′,6-diamidino-2-phenylindole, ThermoFisher, UK)-PBS solution. The pre-osteoblasts were observed with fluorescent microscopy (Nikon Ti Eclipse, Japan). Cellular interactions with the micro-porosity were observed using electron microscopy (as above) after fixating the cells using a procedure reported elsewhere[15].

Cellular volume and extent of differentiation were quantified by means of DNA, protein content and Alkaline Phosphatase levels measurement on the cell lysates. A cell lysate was obtained by removing samples from culture at pre-determined timepoints (day-14, -21, -28), washing them with PBS (Gibco, UK) three times and submerging them in 500 μL of 0.1% Triton-X (Sigma-Aldrich, UK) diluted in DNA-free water (Fisher Scientific, UK). These samples were stored at -80 °C prior to analysis. A cyclical quintuplicate of freeze-thaw cycles were conducted to ensure proper cell lysis, after which the cell lysate was collected and

transferred to a 1.5 mL Eppendorf. DNA content was quantified using the Quanti-iT^{TM} PicoGreen® dsDNA Assay Kit (Thermofisher, UK). This applies an ultrasensitive fluorescent nucleic acid stain to bind to dsDNA, forming a highly fluorescent complex to quantify as little as 25 pg/mL of dsDNA. 25 μL of each cell lysate solution were mixed with 75 μL of 1X Tris-EDTA buffer solution in a black, clear-bottom 96-well plate. 100 μL of PicoGreen® solution (prepared as per the manufacturer's protocol) were added to each sample well and left to incubate (at room temperature) for 5 min in the absence of light, after which fluorescence analysis was completed using a spectrophotometer (Ex:480/Em:520). Fluorescence values obtained were then quantified into DNA content, via the use of a previously prepared DNA standard curve, following the manufacturer's protocol.

The protein content of pre-osteoblasts, indicative of cellular volume, was quantified using the Pierce^{TM} 660 nm reagent (Sigma Aldrich, UK). This method utilises the binding of a metallic dye complex (brown in colour) to proteins that results in a deprotonation of the dye that subsequently shifts colour to green in acidic conditions. 10 μL of cell lysate was pipetted into a black, clear-bottom 96-well plate, after which 150 μL of Pierce^{TM} reagent were added, left to incubate for 5 min and absorbance reading obtained (660 nm). Protein content was normalised by the DNA content and was therefore relative to the protein content per cell on each sample.

ALP content, a key indicator of osteoinduction, was quantified using the 4-MUP reaction. 4-MUP is a fluorescent substrate for ALP and turns blue once phosphorylated. This reaction can be halted by the addition of Tris-EDTA buffer solution. 50 μL of cell lysate were pipetted into a black, clear-bottom 96-well plate, diluted by 50 μL of dH_20, and followed finally by the addition of 50 μL of 4-MUP solution, this was left to incubate (at room temperature) for 30 min. 50 μL of 100 mM Tris-EDTA (Sigma-Aldrich) were then added to stop the reaction.

Finally, florescence was measured using a spectrophotometer (Ex:360/Em:440). ALP content was normalised by the DNA content and was therefore relative to the ALP content per cell on each sample.

2.6. Statistical Analysis

Measurements were completed in quadruplicate (n=4) unless otherwise stated. Statistical analysis was performed using GraphPad Prism (v9.1). Statistical significance in the comparison of as-designed and as-manufactured scaffolds was conducted using a two-tailed t-test. Normality of data distribution in the biological results was confirmed using the Shapiro-Wilk Normality Test and any significant difference in data was detected using a one-way ANOVA, with Fisher's LSD Multiple Comparison post-hoc test. When data did not conform to normal distribution, significance was instead determined using a Kruskal-Wallis test, with Dunn's Multiple Comparison post-hoc test. The threshold for statistical significance was set at $p < 0.05$.

3. Results and Discussion

3.1. Design of scaffolds

The study intent was to control surface area within a range across all topologies for comparative purposes. Because this depends on porosity, the design work focused on the effect that unit-cell number had on surface area when the as-designed porosity was kept constant. As it is well-known that the actual porosity of SLM scaffolds is lower than the as-designed porosity [12, 16], an iterative study to quantify the decrease of the actual porosity on the as-printed scaffolds was carried out (**Figure 2**). For this purpose, preliminary specimens in the five designs were prepared and measured in CAD (as-designed, solid squares in Figure 2) and prediction lines were drawn to locate the interpolated unit-cell number that would yield

the desired surface area per volume ratio. The specimens were then manufactured, and their 'dry' porosity measured (as-manufactured actual porosity, blank squares in Figure 2), which allowed a prediction of the surface-area-to-volume ratio value, accounting for the effects of SLM manufacturing. These preliminary studies informed that the manufactured T-Sharp set would incur a further decrease of the surface area, hence the initial designed porosity was slightly higher than the rest (Figure 2d). It was determined that the as-designed TPMS-Gyroid structure required 216 unit-cells, TPMS-IWP 125 unit-cells, T-Smooth and T-Sharp 833 unit-cells, and Cubic-lattice 1728 unit-cells.

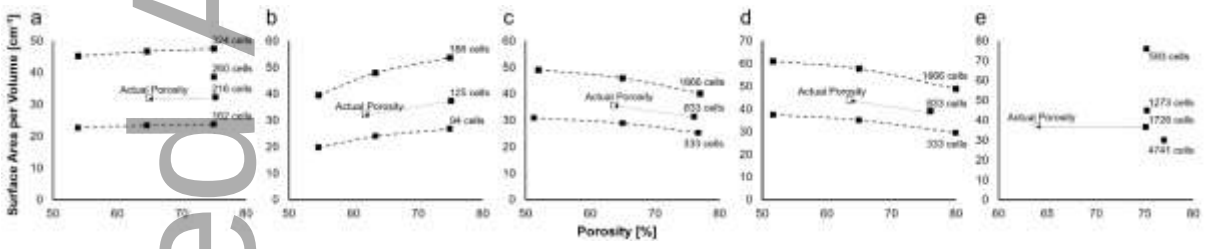

Figure 2. Surface-area-per-volume values as a function of porosity for as-designed (black squares) and as-manufactured (blank squares) scaffolds a) TPMS-Gyroid, b) TPMS-IWP, c) T-Smooth, d) T-Sharp, e) Cubic Lattice, allowing prediction of decrease in actual porosity in the as-manufactured scaffolds. This tool allows the selection of unit-cell number in the initial CAD designs.

3.2. Characterisation of models and scaffolds

The measurements of porosity, pore size, strut size, surface area (reported as the surface area to total volume ratio) and wall roughness (measured on the reconstructed volumes from μCT) on the as-designed CAD models and the as-manufactured printed scaffolds are presented in **Table 1**. Results obtained from Gaussian curvature can be found in Supporting information. A visual comparison between the as-designed and as-manufactured and reconstructed

scaffolds is presented in **Figure 3**. The disparities presented in the porosity indicate that the target porosity was not achieved with the SLM printed scaffolds, despite the compensation efforts described in section 3.1. This was expected as it has been widely reported in literature [12-13, 16]. While the Archimedes's method (using Acetone as immersion medium) has been reported to yield very accurate results [17], the departure of the actual porosity from the design intent is clear. The pore sizes were smaller in the as-manufactured TPMS samples, resulting in a decrease of actual porosity. The wall thickness was wider in the sheet-based TPMS scaffolds, but the strut size narrower in the strut-based scaffolds (i.e., T-Smooth, T-Sharp and the Cubic Lattice). This narrowing is thought to be related to the laser beam creating a thinner strut because the offset parameter, intended to ensure that the edge of the melt pool matches the CAD geometry, was over-compensated and thereby created thinner material beams, in particular the struts parallel to the build direction. The widening of the struts or sheets have been also reported elsewhere and are due to parasitic mass at the curb struts or corners and over-melting of the particles [18] and differences in heat transport between the powder and the solid material, leading to the loose powder sintered to the surfaces [16]. It has also been observed that the extra materials are mostly distributed in the places perpendicular to the building orientation [19], and this was also seen in the printed samples (esp. Cubic Lattice scaffolds in Figure 3e, front row). There were no statistical differences between as-designed and as-manufactured pore sizes (Table 1), indicating that the discrepancies are independent of topology design and intrinsic to the manufacturing process. However, there is statistical significance in the Gyroid's and Cubic Lattice's strut (or wall) thickness, strongest in the latter, indicating that the deposition of the extra materials is more prevalent in that topology design, supporting the statement above.

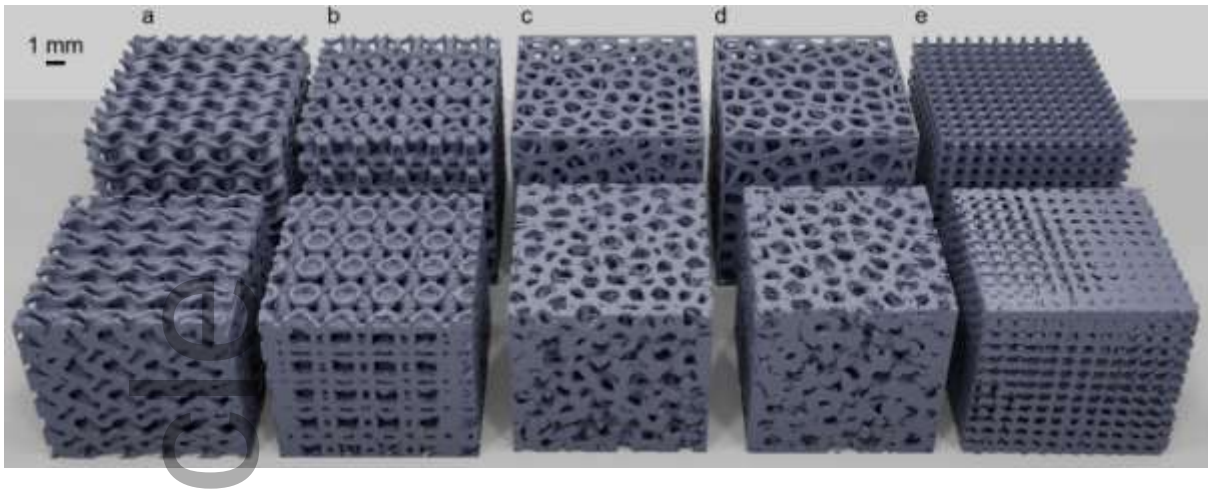

Figure 3. a) TPMS-Gyroid, b) TPMS-IWP, c) T-Smooth, d) T-Sharp, e) Cubic Lattice (back row) CAD designs and (front row) printed and reconstructed scaffolds depicting surface roughness and imperfections incurred in the manufacturing process.

Table 1. Physical characteristics of the scaffolds as-designed models (CAD) and as-manufactured scaffolds (including features measured in the reconstructed volumes from μCT)

[appears at the end of the document]

3.2.1. Surface area and wall roughness

The surface area (normalised by volume, cm^{-1}) measured on the as-manufactured scaffolds was larger than the design intent, despite attempts made to predict it, as explained in the section 3.1. A decrease in porosity (actual vs design) derives a decrease in surface area for the TPMS and an increase for the trabecular-like ones, as depicted in Figure 2. A decrease in unit-cell number decreased the surface area in Cubic Lattice structures. However, the increase in surface area in the as-manufactured scaffolds was of a larger magnitude than expected (see Table 1, surface area/volume). A fractal effect emanating from the wall roughness produced

by the presence of partly-sintered particles is thought to be a major contributor to this. The presence of satellite and (partly-)melted cpTi particles (known as 'secondary roughness' [20] and widely reported in porous structures processed by SLM [16a, 21]) on the walls and struts of all the structures (**Figure 4**a-c) created a microscale roughness, as well as contributing to the decrease in actual porosity (compared to the as-designed porosity) (Figure 4f-j). Corner and strut-joint occlusion was particularly marked in strut-based T-Sharp and Cubic Lattice scaffolds (Figure 4i-j). This secondary roughness did not deter pre-osteoblastic attachment (Figure 4d,e). There were no statistical differences in the roughness of the reconstructed as-manufactured among the different topologies (Table 1), adding to the premise that secondary roughness arises independently from topology design and it is intrinsic to the SLM process.

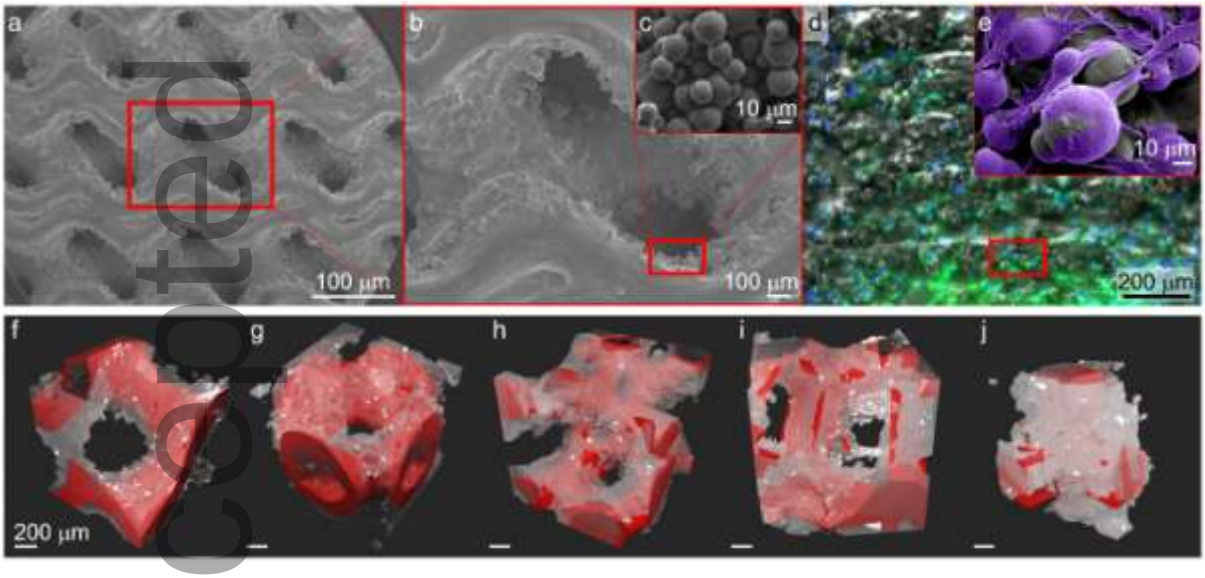

Figure 4. a) SEM observation on a TPMS-Gyroid scaffold (middle plane), b) and c) zoomed-in details of the previous, d) MC3TE3-C1 pre-osteoblasts deposited on the 'secondary porosity' of a cpTi produced by SLM using the laser parameters in this study, e) zoomed-in details of the previous. After 24 h, the pre-osteoblasts present extended pseudopods that attach well to the substrate and spread over large areas. The pre-osteoblasts have been stained to display their nucleus (blue) and membrane (green) under fluorescent light (in d), and in purple to distinguish them from the partly-sintered powder (in e). Discrepancies study:

superposition of printed, μCT scan and reconstructed (grey) unit-cells over CAD designs (red) to show discrepancies in the as-manufactured scaffolds due to the presence of 'secondary roughness' (i.e., partly-melted cpTi particles) in the f) TPMS-Gyroid, g) TPMS-IWP, h) T-Smooth, i) T-Sharp, j) Cubic Lattice.

The contour size (i.e., roughness) values measured on the reconstructed μCT models of the scaffolds sits in the bracket size 45-50 mm (Table 1), which matches the mean particle size of the raw powdered material and is lower than the pore throat radius (**Figure 5**, inset). This result further confirms the appropriate selection of the resampling factor at the time of volumetric reconstruction. Since this roughness has been reported to impact mechanical performance, esp. as crack initiation sites [22], and surface roughness is a well-known factor driving osteoblastic behaviour [23], further studies on the micro-porosity created by the satellite and partly-sintered particles were performed. Figure 5 presents a size distribution of the throat (or wells) radii created by these sintered particles and the cumulative pore area (per g) of these with respect to the pore throat radii. For pores with a radius 10 μm and larger, there are only small differences between the designs, and there is a positive correlation with porosity, i.e., larger actual (acetone) porosity yields larger cumulative pore areas. Those pores are desirable for essential osteoconduction and vascular tissue ingrowth. There is a switch at 7 μm and at < 6 μm the specific cumulative pore area values diverge. When 1 μm pore throat radii are achieved, the total cumulative pore area increases markedly in the TPMS designs (IWP 108.64 cm^2/g, Gyroid 102.32 cm^2/g total) when compared to the Trabecular designs (T-Smooth 78 cm^2/g, T-Sharp 71 cm^2/g). These small pores, i.e., micro-porosity, attributed to the wall micro-roughness, contribute more to the specific cumulative pore area in the TPMS scaffolds when the pore throat radius is < 7 μm. The cumulative pore area increases sharply

for the IWP, indicating that there are many pores of very small sizes, probably in the IWP 'neck' area of the design, as depicted in the first peak of pore throat radius distribution (Figure 5, inset). On the contrary, the cumulative pore area increases gradually in the T-Sharp, suggesting there are fewer very small pores (Figure 5, inset, < 4 μm). Although the cumulative pore area has been displayed in Figure 5 spanning two orders of magnitude for the radii, it is plausible to restrict the true area available to the pre-osteoblasts using a high and a low boundary. Pre-osteoblasts have been found to bridge gaps only when these are shorter than 200 μm[24] (i.e., equivalent to 100 μm throat radii). While the definition of a low boundary cannot be determined accurately because the pre-osteoblasts cannot be viewed in situ in this study, throat radii ~5 μm is an informed estimation as 10-15 μm is the typical size of pre-osteoblasts dendrites and pseudopodia, used by the cells for attachment and mobility (Figure 4e and as observed elsewhere[5, 11, 25]). The shaded area in Figure 5 draws attention to the larger cumulative pore area at that scale in the T-Smooth scaffolds, presenting an advantage over the other structures, and also displaying wider throats (Figure 5, inset). Increased specific surface area at micron- and sub-micron levels has been reported to have a positive effect on bone-implant fixation ability [5].

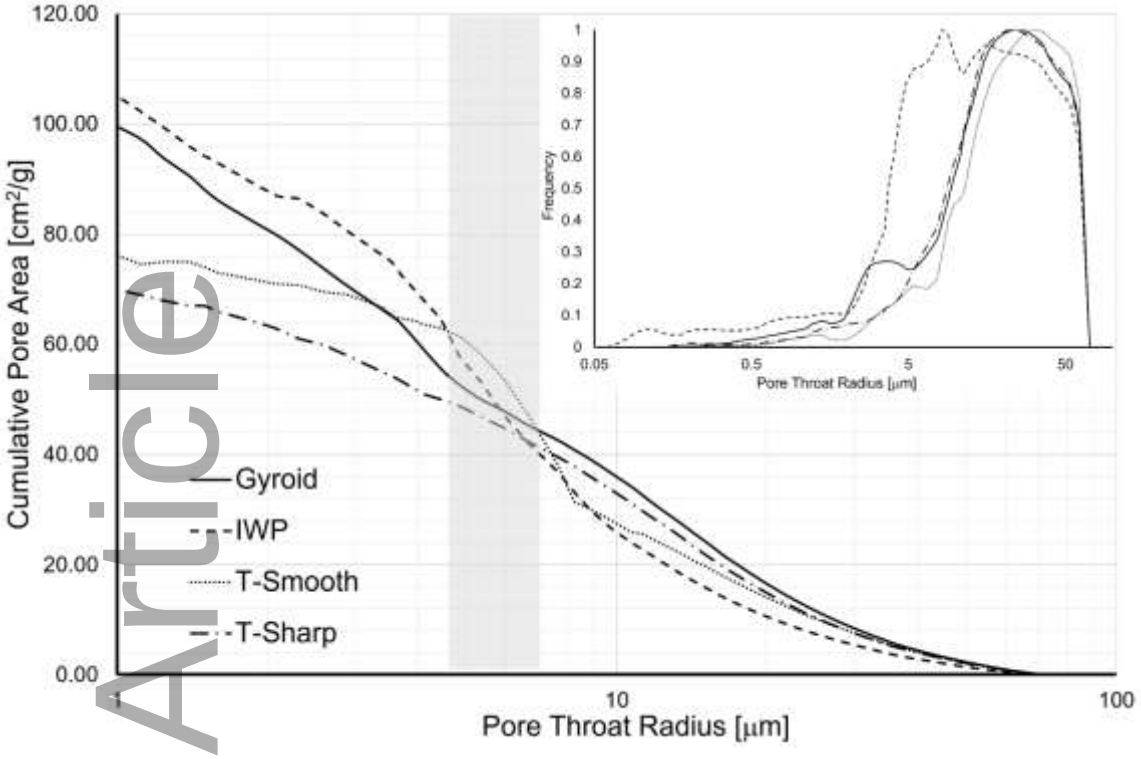

Figure 5. Specific cumulative pore area for the TPMS and trabecular-like scaffolds as a function of pore throat radius and (inset) corresponding pore throat radius distributions. Data collected by mercury porosimetry.

3.3. Compression testing

The scaffolds were subjected to compression testing and the results are presented in Table 1. Stiffness (E_p) is similar in all porous scaffolds, with the Cubic-Lattice situated on the upper boundary and the T-Sharp on the bottom boundary, including SD values. This is expected since the spread of apparent actual densities (or porosities) is narrow, and it has been well documented that density is the major driver to changes in stiffness [7c, 26], despite different pore topology. For instance, the compressive properties exhibited by these TPMS-Gyroid and -IWP are very similar, and this is in agreement with the comparative results obtained on these topologies albeit for a different raw material [26d]. Yield strength of the porous scaffolds (σ_p) is

also similar in all cases and there is even less variation from design to design when considering SD. It is also the case that relative strength is strongly influenced by relative densities [26d, 27]. The strain at yield (ε_p) also follows a narrow range, with the T-Sharp setting the upper boundary and therefore appearing to be the most compliant of the set, and the Cubic-Lattice being on the lower boundary, being the least compliant. The stiffness, yield strength and strain values appear aligned to others reported in literature, though caution must be exercised when comparing different materials (e.g., Ti6V4Al [26b]), actual porosities (e.g., [7c, 16a]), and strut size or sheet thickness [12]. The trabecular designs' (T-Smooth and T-Sharp) stiffness and yield strength results aligned very well to the trabecular bone's exponential relationship reported in [28], confirming mechano-biomimetic properties. The T-Sharp displayed a lower compressive stiffness and yield strength than the T-Smooth. It is hypothesised that the larger levels of irregularity in the structure realised by the deposit of sintered particles in the sharp bends (Figure 4i), described as crack initiation sites, could be behind this effect, because a similar effect has been reported in highly irregular trabecular-like topologies[16a]. Observations made for the DIC videos report a homogeneous distribution of load across the XY plane at yield points for the TPMS designs (**Figure 6**a-b), as expected from other reports: sheet-based Gyroids have been reported to transfer uniform load through helical substructures along the vertical axis [29] and IWP deforms collectively[26d]. The trabecular T-Smooth and T-Sharp designs displayed a similar deformation pattern (Figure 6c-d) with the T-Sharp progressing through compression at a faster pace compared to the T-Smooth. At yield point there is still little evidence of shear planes and the strain map only displays a few compression 'cold spots' (in blue). On the contrary, the Cubic-Lattice (Figure 6e) displays an asymmetric compression along the XY plane. The compressed pores acted as localized stress concentration areas and formed a shear band above which there are examples of buckling and bending. This is attributed to printing imperfections, that the cubic lattice is

prone to (Figure 3e), which can cause failure mode transitions [30]. Figure 6f-j depicts the final state of the samples after Ultimate Compressive Stress, or collapse, whichever was reached first, and inform about their failure modes, very different because these are highly dependent on unit-cell topology [26d]. TPMS-Gyroid and -IWP presented barrelling, in agreement with other studies [12] and exacerbated by the high friction against the platen due to the sandwich structure, and showed an overall shrinkage of the unit-cells, without preferred orientation for deformation and in the absence of shear band formation. This stretching-dominated behaviour result agrees with other studies reported in literature for Gyroid [26b] and IWP [30b] structures. The T-Smooth and -Sharp presented a double shear plane at 45° upon collapse, forming an inverted 'V'. The Cubic-lattice configuration displayed a catastrophic collapse of the middle layers after the deformation strain continued beyond yield point. Those layers collapsed provoking fracture of the sample (Figure 6j). This failure mechanism has been reported in other lattice structures, as it has been demonstrated that although the compressive modulus is larger in the Cubic-Lattice than in, e.g., TPMS-Gyroid, its shear modulus is lowest[6]. The results from this study agree with that statement. For the trabecular-like topologies, the formation of shear bands has been described in the failure mode of strut-based lattice structures [30b, 31].

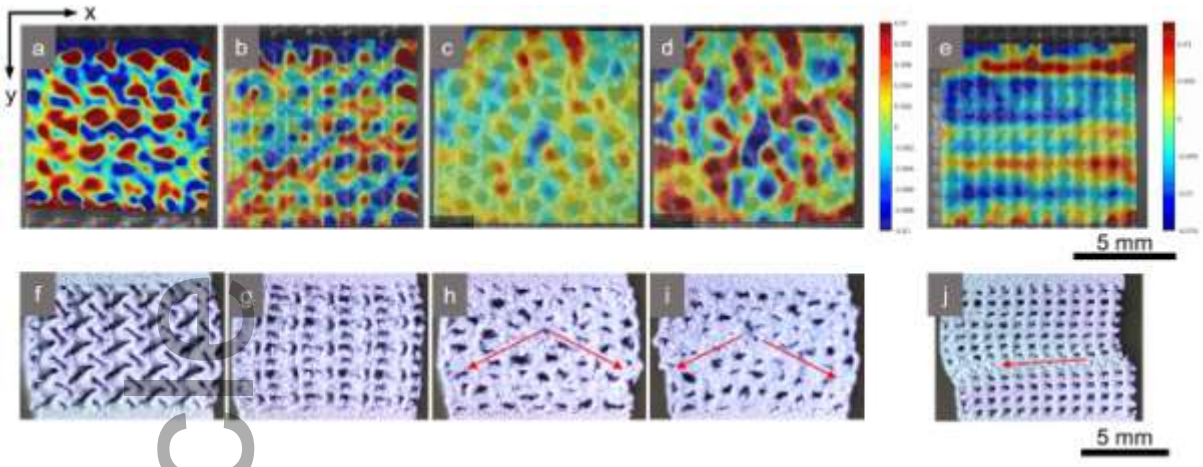

Figure 6. Strain maps (expressed in mm/mm) for the a) Gyroid, b) IWP, c) T-Smooth, d) T-Sharp, e) Cubic Lattice on the XY plane at yield points; and images of the scaffolds after full compressive deformation f) Gyroid), g) IWP, and after collapse h) T-Smooth, i) T-Sharp, j) Cubic Lattice. Arrows depict orientation and direction of the shear planes.

3.4. Biological results from the in vitro studies

A retention study (i.e., cell attachment) was performed at 24 h after seeding to assess any differences in seeding efficiency amongst the different scaffolds structure (**Figure 7**a). The results show that at the early stage of attachment onto the scaffolds, the T-Sharp presented a slight advantage when compared to the other structures, albeit statistical significance is only with the Cubic-Lattice. The Cubic-Lattice topology was the lowest of the entire set and displayed cell attrition, with cells percolating fully through the open, through-hole structure offering less resistance to the cell suspension and with little oblique surfaces for the pre-osteoblasts to attach to. This phenomenon has been reported in other cubic lattices [32] and open strut-foam [25a] configurations. Permeability is therefore an important parameter at the very early stages of the in vitro study. The Cubic-Lattice topology has been reported to have higher permeability than TPMS structures [6], and when comparing Gyroid to IWP, the former has higher permeability[12], which could explain its lower retention with respect to IWP. The T-Sharp scaffolds presented a large amount of sintered and partly-melted particles, esp. in the

corners and joints (Figure 4i), and this could explain why its cell retention is larger, since it has been reported that osteoblasts are better retained onto secondary roughness surfaces [33].

Metabolic activity monitored over 13 days gave an indication of proliferation within the scaffolds (Figure 7b). Pre-osteoblasts proliferated in all the scaffolds, indicating no cytotoxicity in the environment for them. Cell numbers on the T-Sharp scaffolds were higher for the first 7 days, and although there are not statistically significant differences in the results except for day 1, this performance could be attributed to the shorter radius of curvature, which makes it more concave, in the strut joints in this structure, subjected to concavity-driven growth acceleration [34]. However, after day 9, except for Cubic-Lattice, cell growth was arrested and phenotype switched, as expected in this cell line [35]. It is by days 11-13 (Figure 7c) that Cubic-Lattice achieved that, and this delay is assumed to be due to the higher attrition and lower cell numbers in the structure from the outset and therefore a longer time required to reach cell cycle exit conditions. Subsequent increases in cell number are indicative of an increased metabolic activity of senescent maturing cells accommodating higher metabolic activity derived from extra-cellular matrix (ECM) production.

The differentiation study commenced at day 14 in the cell-laden scaffolds, having confirmed the pre-osteoblastic phenotypical switch on all scaffolds by that time point. The study was carried out over 28 days to recapitulate a more physiologically relevant in vitro model that results in more translation-ready pre-clinical data. The DNA content (Figure 7d), indicative of cell number, does not show any significant difference, and the data displays large variability. This is indicative of a cellular non-proliferative stage, as expected beyond day 14. By day 28, DNA values are equal or lower than in previous time points, indicating cell number decay due to suspected apoptosis. Protein content values are indicative of cell volume [36], and, when normalised by DNA content, of cellular population morphology (Figure 7e). During long-term culture periods, osteoblasts can go through periods of hypertrophy (i.e., an increase in

protein concentration without cellular proliferation) or hyperplasia (i.e., a decrease in matrix protein production). In this study the volume of osteoblasts cultured in all scaffolds, except in T-Sharp, were positively correlated with study duration, indicating production of matrix proteins. Hypertrophy of the osteoblasts in Cubic-Lattice by day 28, with statistical differences, could be explained by the mechanical stimuli experienced by the osteoblasts spanning across corners, which have been reported to promote volume augmentation [32] and commitment towards osteogenesis. On the contrary, hyperplasia observed in the osteoblasts incubated in T-Smooth could be a response to a decreased metabolic demand due to the completion of a specialised function, such as differentiation. This hypothesis was validated by further investigation of ALP expression.

ALP levels, normalised by DNA content to indicate cellular population maturity (Figure 7f), from osteoblasts cultured on the TPMS scaffolds show TPMS-IWP upregulated this maturation marker to a larger extent than TPMS-Gyroid, with significant differences except for day 14. The ALP levels in T-Smooth structures appear upregulated with significant differences, except for day 14 (without statistical significance) compared to the T-Sharp. This effect is attributed to the larger pore sizes, larger surface areas and larger cumulative pore areas in the TPMS-IWP and T-Smooth with respect to their counterparts. Large pore sizes are reported to accelerate osteoblast maturation[15, 37], although only surface area was measured in [15]. Levels of ALP on the osteoblasts differentiating in the Cubic-Lattices were downregulated with respect to the other scaffolds at all time points. These results reached statistical significance in all cases except for day 21 with the TPMS-Gyroid and T-Sharp, and day 28 with the TPMS-Gyroid, where statistical significance is not reached. A smaller pore size could be the reason for this result, and although ALP levels increased throughout the long-term study, indicating osteoblastogenesis, this design appears to be less conducive to maturation than the rest. A preference for irregularity in strut-based scaffolds by human

osteosarcoma that showed upregulated ALP levels has been reported[16a], however similar data has not been found for MC3T3-E1. With regards to trabecular-like designs, ALP levels on the T-Sharp scaffolds appear stagnant from day 14 to 28, also indicating this structure is the least conducive to osteoblastogenesis, and hindered at day 28 with significant statistical differences when compared to all the other structures. This means that the osteoblasts incubated in this structure were still in early stages of differentiation since ALP activity is an early marker of osteoblast differentiation that peaks just before matrix mineralisation begins. Pore size and strut thickness in the T-Sharp scaffolds are within the range of the values measured in the other structures. However, a very small cumulative pore area in the T-Sharp could be a cause. On the contrary, by day 28 the ALP levels produced by the osteoblasts incubated in the T-Smooth scaffolds appeared markedly upregulated with respect to all the other scaffolds with statistical significance. Incidentally, this structure displays the largest cumulative pore area at the scale of pseudopodia size (the shaded area) in Figure 5 and the wider throat radius (Figure 5, inset). There exists a positive correlation between cumulative pore area value (i.e., micro-porosity) and extent of differentiation by day 28. Therefore, it can be concluded that this is an important design parameter for implantation scaffolds or 3D networks in tissue engineering. Since osteoblasts are known to trigger their differentiation and secretion of ECM by physical cues (namely cell-to-cell direct contact via pseudo-, filo-podia interactions [25a]) and proximity to other cells, it is hypothesised that the T-Sharp's higher concavity at the strut joints and corners, which shortens the strut-to-strut span and therefore is less demanding for the pseudo-, filo-podia stretching over gaps, may have inhibited differentiation extent when compared to the ongoing maturation of the osteoblasts in the other scaffold designs. The preference of osteoblasts for trabecular-like structures to the detriment of TPMS configurations contributes to the argument that TPMS topologies might not after all be convenient to replicate biological

structures since it has been confirmed that trabecular bone does not approximate a minimal surface but exhibits a more intricate curvature landscape[38].

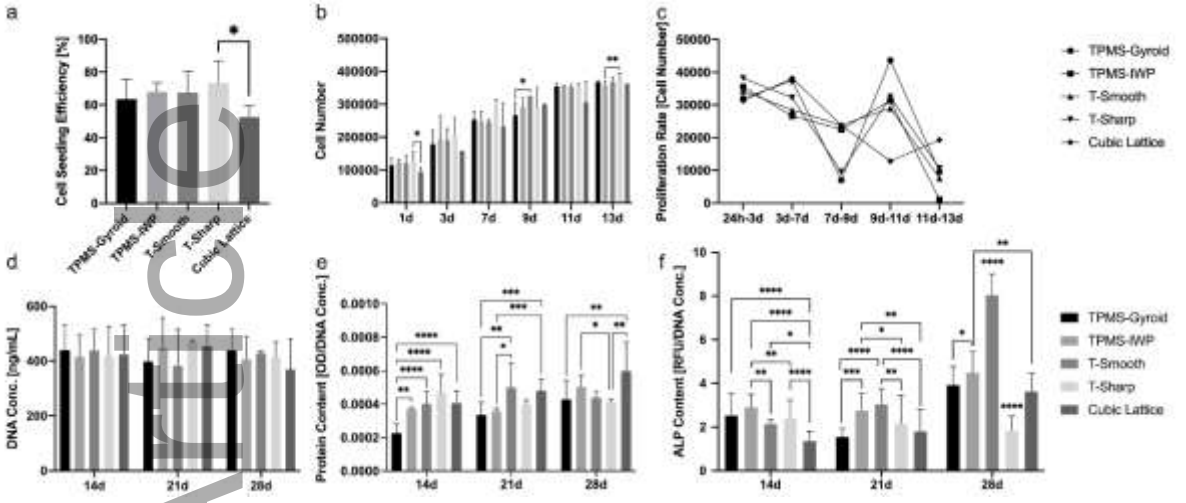

Figure 7. a) Comparative of MC3T3-E1 seeding efficiency at 24 h indicating cell attachment among different scaffolds, b) and c) proliferation study over 13 days reported as absolute cell numbers and rate, respectively, d-f) long term differentiation study reporting on d) DNA content (a surrogate of cell number), e) protein content normalised by DNA, to indicate individual cell volumes, and f) ALP levels as differentiation marker normalised by DNA content. (n=4) Statistical significance: *$p < 0.05$, **$p < 0.01$, ***$p < 0.001$, ****$p < 0.0001$. Lines were used to draw comparisons between topologies, whilst the absence of a line for a marker indicates significance was universal to all other topologies at that timepoint. No marker indicates a lack of statistical significance.

4. Conclusions

Efforts to compensate for discrepancies between the as-designed and as-manufactured SLM cpTi scaffolds were made to control the actual porosities and surface areas-per-unit-volume, important drivers in pre-osteoblastic behaviour. Since these fell within a tight range, topology comparisons independent from them were possible. As a result, the differences in

compression between the TPMS structures were small due to similar apparent porosities, confirming porosity is a dominant factor over topology design. Both TPMS scaffolds displayed uniform stretching-dominated deformation and similar failure mode. In contrast, the Trabecular topologies were more affected by printing imperfections, i.e., partly-sintered particles in corners and joints in the sharper designs, but yielded a stiffer and stronger behaviour than TPMS when the topology was smoothed. Both their failure modes displayed double-shear bands, typical for strut-based lattices.

From a bioengineering viewpoint, the sheet-TPMS and the strut-based lattices sustained cellular attachment with good retention and were prone to osteoblast proliferation and differentiation. The TPMS-IWP performed better than its TPMS-Gyroid counterpart, attributed to a larger surface-area-per-unit-volume and a higher cumulative pore size (micro-porosity). This correlation was not found in the trabecular-like topologies. Despite a lower surface-area-per-unit-volume and lower cumulative pore size, the T-Sharp structure promoted a faster proliferation rate, explained by the concavity-driven effect in cellular growth. However, maturation was hindered. It was the T-Smooth topology, with a larger surface-to-volume-ratio, more accessible pore throats, and larger cumulative pore area at sizes that match osteoblast protrusion geometry, that allowed further extension of osteoblastogenesis over the long-term differentiation study.

The results suggest that, once macro-porosity and pore size values satisfy the minimum requirements of mass transport and mechanical integrity, the most advantageous condition for osteoblastic maturation is offered by a trabecular-like disordered topology with a smoothed finish. The intrinsic roughness generated in the SLM manufacturing process that produced a micro-porosity on the scaffold struts and walls, which particularly favoured the T-Smooth topology, should also not be disregarded but purposely considered as a design feature as it is believed to have been an important contribution to the larger maturation extent obtained in

those scaffolds. Both macro and micro-porosity, known to be important for cell response and fate, should be included in the design of successful medical implants.

Supporting Information
Supporting Information is available from the Wiley Online Library or from the corresponding author.

Conflict of interest
The authors declare no conflict of interest.

Acknowledgements
Authors gratefully acknowledge EPSRC (grant nos. EP/L014998/1, EP/P027482/1, EP/V007335/1) for financial support. Dr J Wang produced the SMEs for Figure 4a-c at the Loughborough Materials Characterisation Centre. Dr E Demirci generated the μCT scans.

Received: ((will be filled in by the editorial staff))
Revised: ((will be filled in by the editorial staff))
Published online: ((will be filled in by the editorial staff))

References

[1] a) G. Bouet, D. Marchat, M. Cruel, L. Malaval, L. Vico, *Tissue engineering. Part B, Reviews* **2015**, 21, 133; b) S. Payr, E. Rosado-Balmayor, T. Tiefenboeck, T. Schuseil, M. Unger, C. Seeliger, M. van Griensven, *Journal of Orthopaedic Surgery and Research* **2021**, 16, 13.

[2] C. Torres-Sanchez, M. Norrito, J. Wang, H. Bell, L. Zani, P. P. Conway, *Surface and Coatings Technology* **2020**, 403, 126439.

[3] G. Ryan, A. Pandit, D. P. Apatsidis, *Biomaterials* **2006**, 27, 2651.

[4] V. Karageorgiou, D. Kaplan, *Biomaterials* **2005**, 26, 5474.

[5] F. A. Shah, P. Thomsen, A. Palmquist, *Acta Biomaterialia* **2019**, 84, 1.

[6] Y. Lu, L. Cheng, Z. Yang, J. Li, H. Zhu, *PLOS ONE* **2020**, 15, e0238471.

[7] a) D. Melancon, Z. S. Bagheri, R. B. Johnston, L. Liu, M. Tanzer, D. Pasini, *Acta Biomaterialia* **2017**, 63, 350; b) M. Dumas, P. Terriault, V. Brailovski, *Materials & Design* **2017**, 121, 383; c) D. Barba, E. Alabort, R. C. Reed, *Acta Biomaterialia* **2019**, 97, 637.

[8] a) S. C. Kapfer, S. T. Hyde, K. Mecke, C. H. Arns, G. E. Schröder-Turk, *Biomaterials* **2011**, 32, 6875; b) O. Al-Ketan, R. Rezgui, R. Rowshan, H. Du, N. X. Fang, R. K. Abu Al-Rub, *Advanced Engineering Materials* **2018**, 20, 1800029.

[9] H. Chen, Q. Han, C. Wang, Y. Liu, B. Chen, J. Wang, *Frontiers in bioengineering and biotechnology* **2020**, 8, 609.

[10] N. Taniguchi, S. Fujibayashi, M. Takemoto, K. Sasaki, B. Otsuki, T. Nakamura, T. Matsushita, T. Kokubo, S. Matsuda, *Materials Science and Engineering: C* **2016**, 59, 690.

[11] P. Ouyang, H. Dong, X. He, X. Cai, Y. Wang, J. Li, H. Li, Z. Jin, *Materials & Design* **2019**, 183, 108151.

[12] F. S. L. Bobbert, K. Lietaert, A. A. Eftekhari, B. Pouran, S. M. Ahmadi, H. Weinans, A. A. Zadpoor, *Acta Biomaterialia* **2017**, 53, 572.

[13] Y. Du, H. Liang, D. Xie, N. Mao, J. Zhao, Z. Tian, C. Wang, L. Shen, *Materials Chemistry and Physics* **2020**, 239, 121968.

[14] J. Schindelin, I. Arganda-Carreras, E. Frise, V. Kaynig, M. Longair, T. Pietzsch, S. Preibisch, C. Rueden, S. Saalfeld, B. Schmid, J.-Y. Tinevez, D. J. White, V. Hartenstein, K. Eliceiri, P. Tomancak, A. Cardona, *Nature Methods* **2012**, 9, 676.

[15] C. Torres-Sanchez, M. Norrito, F. R. Almushref, P. P. Conway, *Materials Science and Engineering: C* **2021**, 124, 112026.

[16] a) H. Liang, Y. Yang, D. Xie, L. Li, N. Mao, C. Wang, Z. Tian, Q. Jiang, L. Shen, *Journal of Materials Science & Technology* **2019**, 35, 1284; b) F. Bartolomeu, N. Dourado, F. Pereira, N. Alves, G. Miranda, F. S. Silva, *Materials Science and Engineering: C* **2020**, 107, 110342.

[17] D. Mahmoud, M. A. Elbestawi, *The International Journal of Advanced Manufacturing Technology* **2019**, 100, 2915.

[18] Z. S. Bagheri, D. Melancon, L. Liu, R. B. Johnston, D. Pasini, *Journal of the Mechanical Behavior of Biomedical Materials* **2017**, 70, 17.

[19] Y. Lu, Z. Cui, L. Cheng, J. Li, Z. Yang, H. Zhu, C. Wu, *Journal of the Mechanical Behavior of Biomedical Materials* **2020**, 112, 104080.

[20] D. Greitemeier, C. Dalle Donne, F. Syassen, J. Eufinger, T. Melz, *Materials Science and Technology* **2016**, 32, 629.

[21] H. Salem, L. N. Carter, M. M. Attallah, H. G. Salem, *Materials Science and Engineering: A* **2019**, 767, 138387.

[22] a) K. F. Walker, Q. Liu, M. Brandt, *International Journal of Fatigue* **2017**, 104, 302; b) I. Koutiri, E. Pessard, P. Peyre, O. Amlou, T. De Terris, *Journal of Materials Processing Technology* **2018**, 255, 536.

[23] a) K. Anselme, P. Linez, M. Bigerelle, D. Le Maguer, A. Le Maguer, P. Hardouin, H. F. Hildebrand, A. Iost, J. M. Leroy, *Biomaterials* **2000**, 21, 1567; b) K. M. Hotchkiss, G. B. Reddy, S. L. Hyzy, Z. Schwartz, B. D. Boyan, R. Olivares-Navarrete, *Acta Biomaterialia* **2016**, 31, 425.

[24] W. Xue, B. V. Krishna, A. Bandyopadhyay, S. Bose, *Acta Biomaterialia* **2007**, 3, 1007.

[25] a) K. C. Nune, R. D. K. Misra, S. M. Gaytan, L. E. Murr, *Journal of Biomedical Materials Research Part A* **2015**, 103, 1677; b) C. Wang, X.-d. Xie, X. Huang, Z.-h. Liang, C.-r. Zhou, *Colloids and Surfaces B: Biointerfaces* **2015**, 132, 1.

[26] a) D. W. Abueidda, R. K. Abu Al-Rub, A. S. Dalaq, D.-W. Lee, K. A. Khan, I. Jasiuk, *Mechanics of Materials* **2016**, 95, 102; b) C. N. Kelly, J. Francovich, S. Julmi, D. Safranski, R. E. Guldberg, H. J. Maier, K. Gall, *Acta Biomaterialia* **2019**, 94, 610; c) C. Torres-Sanchez, J. McLaughlin, R. Bonallo, *Journal of Materials Engineering and Performance* **2018**, 27, 2899; d) O. Al-Ketan, R. Rowshan, R. K. Abu Al-Rub, *Additive Manufacturing* **2018**, 19, 167.

[27] C. Yan, L. Hao, A. Hussein, P. Young, *Journal of the Mechanical Behavior of Biomedical Materials* **2015**, 51, 61.

[28] S. Ghouse, N. Reznikov, O. R. Boughton, S. Babu, K. C. G. Ng, G. Blunn, J. P. Cobb, M. M. Stevens, J. R. T. Jeffers, *Applied Materials Today* **2019**, 15, 377.

[29] D. Downing, A. Jones, M. Brandt, M. Leary, *Materials & Design* **2021**, 197, 109096.

[30] a) L. Liu, P. Kamm, F. García-Moreno, J. Banhart, D. Pasini, *Journal of the Mechanics and Physics of Solids* **2017**, 107, 160; b) O. Al-Ketan, R. K. Abu Al-Rub, R. Rowshan, *Journal of Materials Research* **2018**, 33, 343.

[31] M. Smith, Z. Guan, W. J. Cantwell, *International Journal of Mechanical Sciences* **2013**, 67, 28.

[32] S. Van Bael, Y. C. Chai, S. Truscello, M. Moesen, G. Kerckhofs, H. Van Oosterwyck, J. P. Kruth, J. Schrooten, *Acta Biomater* **2012**, 8, 2824.

[33] B. Wysocki, J. Idaszek, J. Buhagiar, K. Szlązak, T. Brynk, K. J. Kurzydłowski, W. Święszkowski, *Materials Science and Engineering: C* **2019**, 95, 428.

[34] M. Rumpler, A. Woesz, J. W. C. Dunlop, J. T. v. Dongen, P. Fratzl, *Journal of The Royal Society Interface* **2008**, 5, 1173.

[35] L. D. Quarles, D. A. Yohay, L. W. Lever, R. Caton, R. J. Wenstrup, *Journal of bone and mineral research : the official journal of the American Society for Bone and Mineral Research* **1992**, 7, 683.

[36] H. A. Crissman , J. A. Steinkamp *Journal of Cell Biology* **1973**, 59, 766.

[37] K. Kapat, P. K. Srivas, A. P. Rameshbabu, P. P. Maity, S. Jana, J. Dutta, P. Majumdar, D. Chakrabarti, S. Dhara, *ACS Applied Materials & Interfaces* **2017**, 9, 39235.

[38] S. J. P. Callens, D. C. Tourolle né Betts, R. Müller, A. A. Zadpoor, *bioRxiv* **2020**, DOI: 10.1101/2020.12.02.4083772020.12.02.408377.

Table 1: Physical characteristics (of the scaffolds as-designed models (CAD) and as-manufactured scaffolds (including features measured in the reconstructed volumes from μCT). (Refers to the 10 x 10 x 10 mm scaffolds)

As-designed				As-manufactured								
Porosity [%]	Pore size ± SD[a] [mm]	Wall thickness or Strut size[a] ± RE[b] [mm]	Surface Area / Volume [1/cm]	Porosity ± SD [%]		Pore size ± SD[d] [mm]	Wall thickness or Strut size[a] ± SD[d] [mm]	Surface Area / Volume ± RE[b] [1/cm]	Contour size (Roughness) on reconstructed volume ± RE[b] [μm]	E_p ± SD[d] [GPa]	σ_p ± SD[a] [MPa]	ε_p ± SD[a] [%]
				Dry[c]	Acetone[a]							

TPMS Gyroid	75	0.81 ± 0.16[0]	0.20 ± 0.01**	32.33	65.66 ± 0.51	71.98 ± 1.80	0.71 ± 0.09[0]	0.26 ± 0.03**	40.48 ± 0.01	48.49 ± 6.48[0]	7.12 ± 1.18	60.22 ± 17.55	1.25 ± 0.29
TPMS IWP	75	1.08 ± 0.12[0]	0.20 ± 0.01[0]	37.37	60.45 ± 0.43	65.61 ± 1.85	1.09 ± 0.16[0]	0.22 ± 0.03[0]	41.41 ± 0.01	51.25 ± 5.34[0]	7.29 ± 0.38	61.66 ± 9.72	1.29 ± 0.15
T-Smooth	76	0.96 ± 0.29[0]	0.41 ± 0.01[0]	33.29	64.03 ± 0.73	67.41 ± 1.93	0.84 ± 0.13[0]	0.35 ± 0.04[0]	55.16 ± 0.01	44.77 ± 5.10[0]	8.20 ± 0.91	66.03 ± 2.69	1.32 ± 0.19
T-Sharp	76	1.04 ± 0.31[0]	0.40 ± 0.01[0]	41.67	63.67 ± 0.55	68.48 ± 1.17	0.80 ± 0.09[0]	0.39 ± 0.07[0]	45.50 ± 0.01	45.53 ± 4.33[0]	5.75 ± 1.27	58.23 ± 4.03	1.45 ± 0.29
Cubic Lattice	76	0.52 ± 0.02[0]	0.44 ± 0.01****	35.27	63.33 ± 1.72	70.23 ± 0.75	0.43 ± 0.09[0]	0.34 ± 0.03****	43.91 ± 0.01	47.04 ± 6.44[0]	9.55 ± 0.71	60.26 ± 4.90	1.05 ± 0.14

[a]n=4

[b]RE = Rounding error. Unlike SD (standard deviation), uncertainty was used as the rounding error because these values were taken from an algorithm and not measured multiple times.

[c]n=8

[d]n=5

Statistical significance: [0]p>0.05, *p < 0.05, **p < 0.01, ***p < 0.001, ****p < 0.0001

ToC

TPMS and trabecular-like structures are common approaches to bone implant design. There is a lack of comparative studies that assess the impact of topology on biological and mechanical performance independent of porosity and surface area. Here these two features are controlled, despite design-to-manufacture disparities intrinsic to SLM. Smoothed Trabecular scaffolds, with more accessible throats lined with a microporosity, enhance osteoblastogenesis.

Carmen Torres-Sanchez*, James M. Borgman, Ben Sargeant, Hugo Bell, Enrique Alabort, Craig Lindsay, Paul P. Conway

Comparison of SLM cpTi sheet-TPMS and trabecular-like strut-based scaffolds for tissue engineering